

Stark many-body localization on a superconducting quantum processor

Qiujiang Guo,^{1,*} Chen Cheng,^{2,3,*} Hekang Li,^{1,*} Shibo Xu,¹ Pengfei Zhang,¹ Zhen Wang,¹ Chao Song,¹ Wuxin Liu,¹ Wenhui Ren,¹ Hang Dong,¹ Rubem Mondaini,^{3,†} and H. Wang^{1,‡}

¹*Interdisciplinary Center for Quantum Information,
State Key Laboratory of Modern Optical Instrumentation,
and Zhejiang Province Key Laboratory of Quantum Technology and Device,
Department of Physics, Zhejiang University, Hangzhou 310027, China*

²*School of Physical Science and Technology, Lanzhou University, Lanzhou 730000, China*

³*Beijing Computational Science Research Center, Beijing 100094, China*

Quantum emulators, owing to their large degree of tunability and control, allow the observation of fine aspects of closed quantum many-body systems, as either the regime where thermalization takes place or when it is halted by the presence of disorder. The latter, dubbed many-body localization (MBL) phenomenon, describes the non-ergodic behavior that is dynamically identified by the preservation of local information and slow entanglement growth. Here, we provide a precise observation of this same phenomenology in the case the onsite energy landscape is not disordered, but rather linearly varied, emulating the Stark MBL. To this end, we construct a quantum device composed of thirty-two superconducting qubits, faithfully reproducing the relaxation dynamics of a non-integrable spin model. Our results describe the real-time evolution at sizes that surpass what is currently attainable by exact simulations in classical computers, signaling the onset of quantum advantage, thus bridging the way for quantum computation as a resource for solving out-of-equilibrium many-body problems.

A fundamental characteristic of much sought-after quantum computers, setting them apart from digital classical computers, is their ability of simulating the dynamics of highly entangled many-particle quantum systems [1]. As a consequence, emulating the non-equilibrium dynamics of many-body systems represents one of the greatest strengths of quantum simulators [2]. In the pursuit of building a fully programmable, and fault-tolerant, digital quantum processor, i.e., a flexible gate-based quantum circuit, other *hybrid* (and simpler) platforms have been thriving. Among those, are the superconducting circuits, which by featuring single- and two-qubit gates, with further in-situ knobs to program various system Hamiltonians, represent a quantum *analog* simulator with the potential to bridge the gap between the most advanced existing supercomputers and the yet elusive digital quantum computer [3, 4]. Here, we provide a concrete example of such quantum advantage, by emulating the dynamics of a quantum system exhibiting both thermalization and its breakdown, depending on the strength of a nonrandom potential, for system sizes that *exact* methods in classical computers cannot compete with.

In particular, the advantage is clearly highlighted by a quick comparison with similar effort that would be demanded on standard computers. For example, for a 32-qubits device, storing the information related to the excitation preserving wave-function requires memory capacities slightly shy of 10 gigabytes. It certainly does not sound dramatic given the current computational capabilities, but to exactly obtain such wave-function, governed by the unitary evolution of some Hamiltonian of interest, *all* of its eigenstates may possess a finite con-

tribution. Thus, the 10 gigabytes requirement needs to be multiplied by the size of the corresponding Hilbert space, shooting up the needed memory to approximately 3 exabytes, more than 500 times of what is available at the largest supercomputer to date [5]. Not to mention the computational time associated to obtaining the eigenstates themselves, with algorithms that scale polynomially with the size of the Hilbert space, ultimately rendering the overall computation unpractical [6].

In the specific isolated generic quantum system we are interested in, the eigenstate thermalization hypothesis [7, 8] provides a framework, based on the random matrix theory and quantum chaos [9], that explains how the expectation value of physical observables at long times gets reconciled with their corresponding thermodynamic averages [10, 11]. As a result, the system's out-of-equilibrium evolution progresses in a manner to scramble local information encoded in the initialization over time, erasing memory of the initial conditions when approaching equilibration, even if unaided by an external reservoir [12–14].

Nonetheless, this generic scenario can break down in the presence of added ingredients, ensuing non-ergodic behavior. The most common one is quenched disorder, wherein by the introduction of randomness on the Hamiltonian of interest, thermalization can be prevented. This is manifested by the localization of the wave functions in Hilbert space, which, in physical terms, results in the halting of mass and energy transport [15–17]. Termed many-body localization (MBL), it has its roots on the non-ergodicity of noninteracting particles in disordered environments, initially introduced by P. W. Anderson [18]. Analytical [19, 20], numerical [21–25] and

experimental [26–35] evidence indicates though its persistence in the presence of interactions, if disorder is sufficiently large.

Further theoretical support also pointed out different mechanisms in which *clean* systems, i.e., without an explicit random component, can either display prethermalization or localization akin to the MBL phenomenon [36–38]. Among them, one is related to the many-body version of a well known single-particle localization process, the Wannier-Stark localization [39, 40], wherein particles in a lattice, subjected to an extra linear potential, become localized, displaying quasi-exponentially localized wave functions [41]. If including interactions, recent numerical studies [41–44] have suggested the absence of thermalization, with indicators precisely similar to the standard MBL, without relying, however, on the original ℓ -bits picture that explains the appearance of local integrals of motion emerging at strong disorder values.

In the language of quantum chaos, our results demonstrate the transition from non-integrability to an emergent one, as the strength of the Stark potential is enhanced, intrinsically related to a fragmentation of the associated Hilbert space [45]. Deep in the non-ergodic phase, long-lived Bloch oscillations are re-identified, reemphasizing the non-thermal aspects of our emulation, and its connections with other experimental indications in cold atoms [46]. Furthermore, from a technological viewpoint, the argument that the MBL phenomenon may be potentially used as a building block for a quantum memory device, becomes more compelling if no explicit disorder is involved, but rather a precise (and often reproducible) linear variation of the energies. The experimental observation of such phenomenon, Stark many-body localization, is one of the main results of our study.

Experimental platform and protocol.— We construct an $N = 32$ qubit quantum analog processor, using transmon superconducting qubits. With the aid of individual control lines, we program 29 of them, with initializations promoted via microwave photon excitations [47]. Their coupling, a mixture of direct and resonator mediated one, describes the effective Hamiltonian [31, 48]:

$$\frac{H}{\hbar} = \sum_{\{i,j\} \in N} J_{ij} (\sigma_i^+ \sigma_j^- + \sigma_i^- \sigma_j^+) + \sum_{j \in N} W_j \sigma_j^+ \sigma_j^-. \quad (1)$$

Here, σ_i^+ (σ_i^-) is the raising (lowering) operator for qubit Q_i , and the first term runs at pairs of qubits Q_i and Q_j . Their disposition, accompanied by the qubit-qubit engineered couplings J_{ij} , is made such that they emulate a typical non-integrable spin-1/2 model on a triangular ladder (or equivalently, a chain with nearest and next-nearest exchange terms, see Fig. 1). Combined with a local adjustment of the resonant frequency for each qubit [47], the second term in (1), it flexibly allows the construction of numerous potential landscapes $\{W_j\}$,

e.g., a linear one, $W_j = -j\gamma$, mimicking a Stark term.

The experiment is performed via the dynamical characterization after an initialization of the qubits, by preparing initial product states via π -pulse excitation on N_\bullet selected ones, while keeping N_\circ -qubits in their ground state. We probe the largest Hilbert space \mathcal{N} with a given conserved number of excitations, by choosing $N_\bullet = N/2$, thus amounting to a total of $\mathcal{N} = 77,558,760$ states. For a finite Stark potential γ , we select $k = 20$ initial states $|\Psi_0\rangle$, carefully chosen to display associated energies $E = \langle \Psi_0 | H | \Psi_0 \rangle$ residing close to the center of the eigenspectrum of (1) (See SM [47]). In the absence of disorder, the average of the dynamical observables for different initializations, and repetitions for each of them, hence constitutes our *statistical* averaging.

Dynamically probing Stark MBL.— We start by characterizing the onset of Stark MBL with growing potentials γ by reporting the time-dependent Hamming distance [28, 49],

$$\mathcal{HD}(t) = \frac{1}{2} \left(1 - \frac{1}{N} \sum_{i=1}^N \langle \Psi_0 | \sigma_i^z(t) \sigma_i^z(0) | \Psi_0 \rangle \right). \quad (2)$$

Here, $\sigma_i^z(t) = e^{i\frac{H}{\hbar}t} \sigma_i^z(0) e^{-i\frac{H}{\hbar}t}$ is the z -Pauli matrix for qubit Q_i , and \mathcal{HD} quantifies the expectation value of the normalized (by the system size) number of excitation flips that have occurred at time t in relation to the initial state $|\Psi_0\rangle$. A necessary condition for ergodicity is that at long times $\langle \sigma_i^z(t) \sigma_i^z(0) \rangle \rightarrow \langle \sigma_i^z(t) \rangle \langle \sigma_i^z(0) \rangle$, yielding $\mathcal{HD}(t) \rightarrow 0.5$; smaller values thus describe memory of the initial preparations. Figure 2(A) displays this time dependence for various Stark potentials. At $\gamma/2\pi = 1$ MHz, the Hamming distance tends to 0.5 at the largest experimental time, $t = 1000$ ns, corresponding to approximately 23 tunneling times (see SM [47]); it attests that thermalization is achieved in our device within time scales for which evolution is yet coherent. Conversely, at large potentials, memory of the initial conditions persists, with an equilibration of $\mathcal{HD} < 0.5$. This is the first indication of non-ergodic behavior in our system, similar to the MBL phenomenon [28]. A compilation of the Hamming distance values at long-times is shown in Fig. 2(B).

In addition, further characterization of the preservation of local information is given by the asymptotic values of the imbalance, commonly used in either cold atom [26, 27, 29, 33] or superconducting qubit experiments [31, 35]. Since our initial product states have a generic local structure, a generalized imbalance [35], defined as $\mathcal{I}_{\text{gen}} = \sum_{i=1}^N \lambda_i \sigma_i^+ \sigma_i^-$, where $\lambda_i = 1/N_\bullet$ ($-1/N_\circ$) on the i -th qubit initialized to $|1\rangle$ ($|0\rangle$), captures initial local memory. With this construction, $\langle \mathcal{I}_{\text{gen}} \rangle$ is always 1 for the initial state and, similarly to the Hamming distance, it relaxes to a value denoting ergodicity, $\langle \mathcal{I}_{\text{gen}}(t \rightarrow \infty) \rangle = 0$, while it remains finite at arbitrarily long times when localization takes place. Insets in Fig. 2

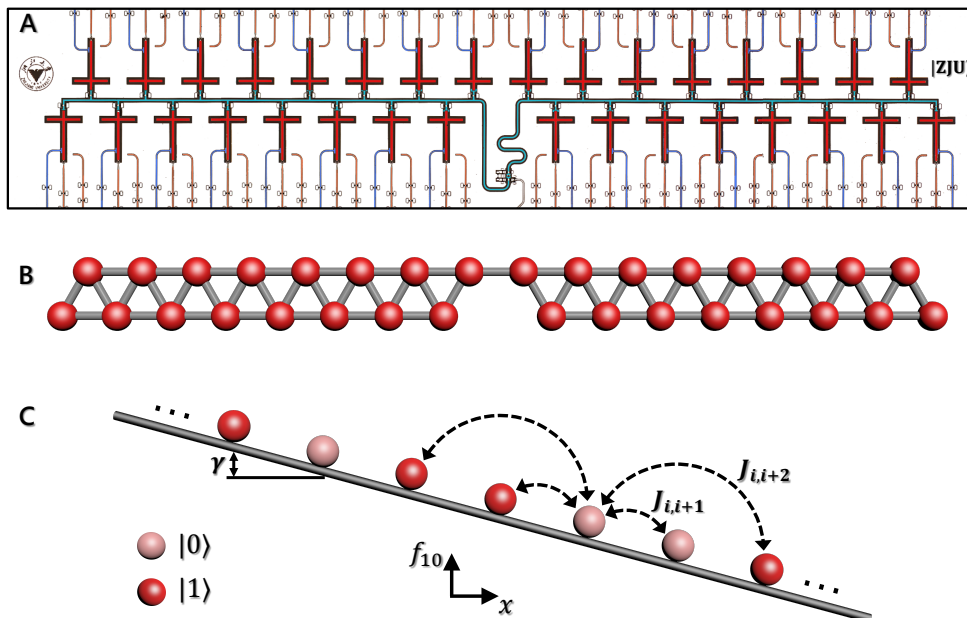


Figure 1. **Quantum processor and schematics of the emulated Hamiltonian.** (A) Optical micrograph of the 32-qubit device, with post-added colors to easily identify the critical circuit elements, as the resonator at the center, control lines and qubits. (B) The schematic representation of the device, with spheres depicting the qubits, and the connecting lines their coupling stemming from the combination of direct- and resonator mediated couplings (See SM for the specific values [47]). (C) A cartoon representation of the Hamiltonian, with a linear potential along the device. This is created by the superposition of the homogeneous offset frequency $|\Delta|$ from the resonator and a second small detuning by a controllable value γ for consecutive qubits along the x -axis, emulating the Stark potential. In the simulations we investigated, half of the qubits are initialized at the excited state $|1\rangle$ via π -pulses, wherein the coherent dynamics is followed, with subsequent measurements occurring at times t after the initialization. When those occur, all qubits are tuned to their respective readout frequencies for simultaneous multi-qubit state measurement.

display the imbalance values at the same parameters used for $\mathcal{H}D$.

Signifying localization via two-body correlations.—

Supporting indication of the onset of localization is also seen via the scaling behavior of two-point correlation functions [4], defined as

$$C(i, j) = |\langle n_i n_j \rangle - \langle n_i \rangle \langle n_j \rangle|, \quad (3)$$

where $n_i \equiv \frac{1}{2}(1 - \sigma_i^z)$ is the local density operator. They form the building block of quantum information theory measurements, as the quantum mutual information [52], shown to display an exponential decay with distance [52, 53] in the MBL phase (thus bounding the decay of any two-point correlation functions), while slower than exponential in the ergodic phase. Figure 3(A) displays measurements for both small ($\gamma/2\pi = 1$ MHz) and large ($\gamma/2\pi = 8$ MHz) potentials, close to their equilibration times for the local observables ($t = 500$ ns), after initializations conducted as before (see SM [47] for snapshots at different times). A growing Stark potential gives rise to very short-ranged correlations at long-times, mostly restricted to nearest-neighbor qubits. On the other hand, a distinctive signature of the large entanglement is obtained at small values of γ , with sizeable $C(i, j)$'s

spread across the device. By averaging all pairs $\{i, j\}$ of distance-equivalent correlations ($\delta x \equiv |i - j|$), we recover the exponential bound $\propto \exp(-\delta x/\xi)$ [Fig. 3(B)], where ξ defines the typical correlation length, which quickly drops with larger Stark potentials [Fig. 3(C)]. Corrections to this functional form in the localized phase [53] may yield a slightly different ξ , but do not change the highly non-local nature of $C(i, j)$ at small γ values.

Stark MBL as opposed to Wannier-Stark localization.— A last pertinent question is whether the observed localization can be distinguished from Wannier-Stark localization [39], a typical single-particle phenomenon. In the latter, unitary dynamics also preserves memory of the initial conditions, challenging its differentiation from the argued many-body localization. However, other dynamical metrics can also discern those, as the growth in time of entanglement measures. In the standard MBL phenomenon, based on the ℓ -bits description of localization, entanglement grows monotonically slow in time as $\propto \log t$ [54, 55], in contrast to Anderson localization, in which it quickly saturates after initial short dynamics [31].

If we carefully select the qubits in our processor which will be put in a coherent state, one can build an effective

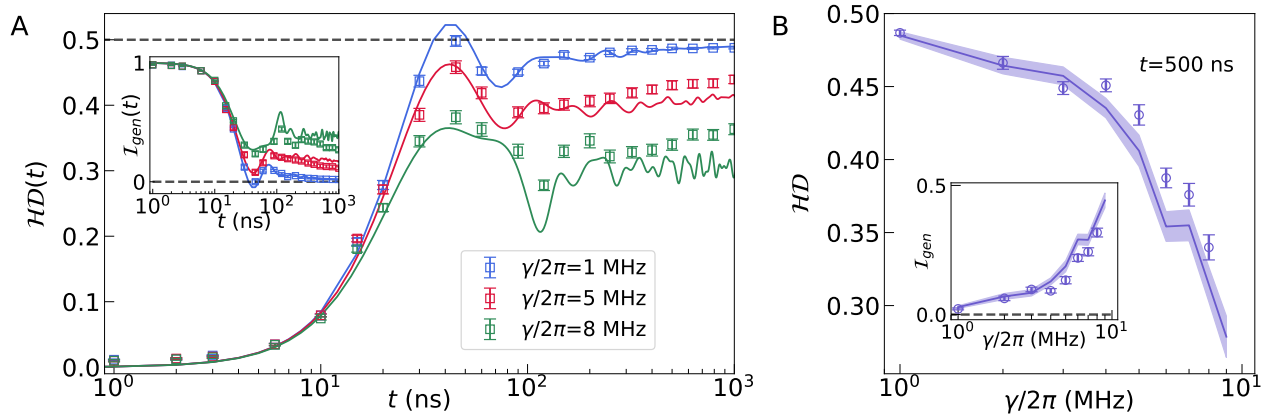


Figure 2. **Relaxation dynamics of few-body observables.** (A) Time-dependent Hamming distance, $\mathcal{H}\mathcal{D}$, with growing Stark potential γ , when using 29 qubits of the device depicted in Fig. 1(A). Averages are taken among $k = 20$ initial states close to the center of the eigenspectrum $\varepsilon \simeq 0.5$. (B) Compilation of Hamming distances at long times; insets in (A) and (B) display similar analysis for the generalized imbalance \mathcal{I} at corresponding γ -values. All data are extracted close to their equilibration values, $t = 500$ ns. Further comparison of the experimental results (markers) with the ones obtained from numerical simulations (lines) is also shown. These employ the time-dependent variational principle (TDVP) [50, 51], in which a matrix product state representation of $|\Psi_t\rangle = e^{-\frac{i}{\hbar}Ht}|\Psi_0\rangle$, bounded by the bond-dimension χ , can be obtained (see SM [47]). The simulation results become increasingly more expensive when approaching thermalization, due to the growing χ necessary to faithfully describe $|\Psi_t\rangle$. Error bars (experiment) and shaded regions (simulation) denote the standard error of the statistical mean.

linear chain of spins, that cannot be differentiated from non-interacting spinless fermions, after a Jordan-Wigner transformation. Although the half-chain entanglement entropy is an onerous measurement that requires a full quantum state tomography [31], simpler witnesses of entanglement have been used, as the quantum Fisher information (QFI) [28, 35], defined as $\mathcal{F}_Q = 4[\langle \mathcal{I}_{\text{gen}}^2 \rangle - \langle \mathcal{I}_{\text{gen}} \rangle^2]$. Figure 4 contrasts the dynamics of QFI when using 16 of the total number of available qubits, emulating an integrable model, and the original case featuring 29 qubits. The difference in between both results is clear, and goes precisely in confirming the slow logarithm-in-time growth of QFI for the Stark many-body localized case, and the quick saturation for the effective noninteracting Hamiltonian.

Coherent oscillations deep in the Stark MBL regime.— While the picture of ergodicity breaking is already unequivocal, the tunability available in our quantum platform allows the verification of emergent Bloch oscillations deep in the Stark MBL regime [56]. This can be understood from a simple spectral analysis: when $\gamma/\overline{J_{ij}} \gg 1$ ($\overline{J_{ij}}$ is the average of all J_{ij} couplings), the system approaches integrability, and the many-body spectrum is highly degenerate, displaying γ -spaced energy levels between quasi-degenerate clouds of states [47]. Consequently, any few-body observable exhibits oscillations with frequency γ . Figure 5 presents a precise test of this prediction by showing the dynamics of a selection of representative quantities, accompanied by a Fourier analysis of the relevant frequencies ω that describe the real-time oscillations at $\gamma/2\pi = 16$ MHz. Coherent Bloch

fluctuations are observed with $\omega = \gamma$ (and higher harmonics), a result not reproducible at small values of the Stark potential [See Fig. 2(A)], where quantum chaotic behavior predominates, and coherent oscillations are only observed at small time scales instead. This confirms the Stark MBL phenomenon we observe, as one related to an emerging integrability at large γ 's, where the dipole-moment arises as a conserved quantity when $\gamma \rightarrow \infty$ [47]. Yet, an analysis of the ETH indicators establishes that non-ergodic behavior sets in even before fragmentation in the spectrum takes place [47].

Outlook.— Unlike recent experiments using trapped atoms on an optical square lattice with added tilt potential [57], the one-dimensional nature of our emulated problem allows us to experimentally observe Stark MBL, as a phenomenon where emergent integrability is manifest within the coherent time scales available, intimately connected to a fragmentation of the Hilbert space. It is important to highlight that arguments stating that thermalization may eventually occur within the dipole-moment conserving subspaces at the regime $\gamma/\overline{J_{ij}} \gg 1$ [58, 59], may render ineffective thermalization provided marginal local variations in the Stark potential, inherent to any realistic experiment, occur. Nonetheless, the MBL phenomenon itself, has been subject to recent scrutiny, and given the number of qubits we have managed to assemble in our quantum simulator, it opens the possibility for testing existing scaling theories of (many-body) localization, complementing results obtained with classical computers at smaller system sizes [60].

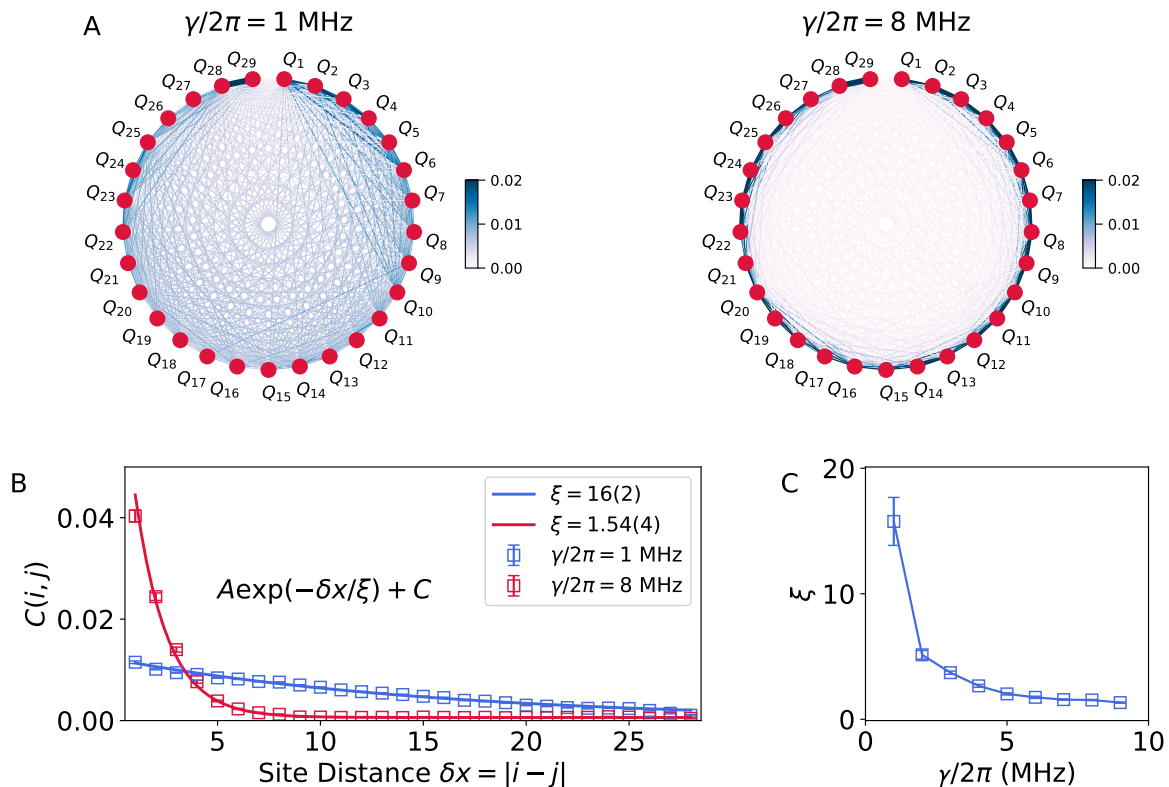


Figure 3. **Ergodicity breaking seen through two-body correlations.** (A) Two-point correlations between all pairs of qubits (Q_i, Q_j) with line color proportional to the correlation strength, at small ($\gamma/2\pi = 1$ MHz) and large ($\gamma/2\pi = 8$ MHz) Stark potential. (B) Averaged two-body correlations $C(i, j)$ across the device as a function of their separation $\delta x \equiv |i - j|$; at small γ 's, all qubits are highly correlated, with a typical correlation length ξ approximately equal to half of the system size. For large tilt potentials, on the other hand, the correlations are much shorter ($\xi \simeq 1$), and the system displays a substantially smaller entanglement. (C) The correlation length extracted from the fitting of the functional form $C(i, j) \propto \exp(-\delta x/\xi) + C$ as a function of γ . Error bars in (B) derive from the $k = 20$ initial state average, and from the fit procedure in (C); all data is extracted at $t = 500$ ns, close to the regime where local observables have already equilibrated.

Note added.— At the completing stages of the manuscript, we learned that recent results in one-dimensional cold atom experiments find non-ergodic behavior due to a tilt potential surviving at relevant experimental time-scales [61], signified by a dynamical memory-preserving scheme, as in our study. Our results verify those, complementing it with entanglement witnesses for a full characterization of the emerging integrability.

Acknowledgments Devices were made at the Micro-Nano Fabrication Center of Zhejiang University. **Funding:** Supported by National Natural Science Foundation of China (Grants No. NSAF-U1930402, 11674021, 11974039, 11851110757, 11725419, and 11904145), National Basic Research Program of China grants (Grants No. 2017YFA0304300 and 2019YFA0308100), and the Zhejiang Province Key Research and Development Program (grant no. 2020C01019). **Author contributions:** C.C. and R.M. proposed the idea; C.C. performed the numerical simulation; Q.G. conducted the experiment; H.L. fabricated the device; R.M., C.C., Q.G., and H.W. co-wrote the manuscript; and all authors contributed to

the experimental setup, discussions of the results, and development of the manuscript. **Competing interests:** Authors declare no competing interests. **Data and materials availability:** All data needed to evaluate the conclusions in the paper are present in the paper or the supplementary materials.

* Those authors contributed equally to this work.

† rmondaini@csrc.ac.cn

‡ hhwang@zju.edu.cn

- [1] J. Preskill, Quantum Computing in the NISQ era and beyond, *Quantum* **2**, 79 (2018).
- [2] E. Altman, K. R. Brown, G. Carleo, L. D. Carr, E. Demler, C. Chin, B. DeMarco, S. E. Economou, M. A. Eriksson, K.-M. C. Fu, M. Greiner, K. R. A. Hazzard, R. G. Hulet, A. J. Kollar, B. L. Lev, M. D. Lukin, R. Ma, X. Mi, S. Misra, C. Monroe, K. Murch, Z. Nazario, K.-K. Ni, A. C. Potter, P. Roushan, M. Saffman, M. Schleier-Smith, I. Siddiqi, R. Simmonds, M. Singh, I. B. Spielman, K. Temme, D. S. Weiss, J. Vuckovic, V. Vuletic, J. Ye,

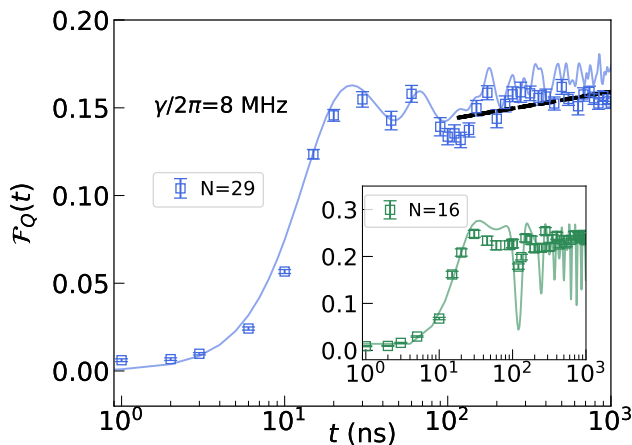


Figure 4. **Entanglement growth – Stark MBL vs. non-interacting localization.** Time dependence of the experimental quantum Fisher information at large tilt potential ($\gamma/2\pi = 8$ MHz). The dashed line depicts a $\log t$ fit of the experimental data in the range $t \in [100, 1000]$ ns, highlighting the growth at long times in the Stark MBL regime. The inset presents the same when selecting just 16 qubits, such as they feature only nearest-neighbor direct couplings, emulating an integrable Hamiltonian. In all data, averages and error bars stem from standard error of the mean of multiple initializations; markers (lines) denote experimental (numerical simulation) data.

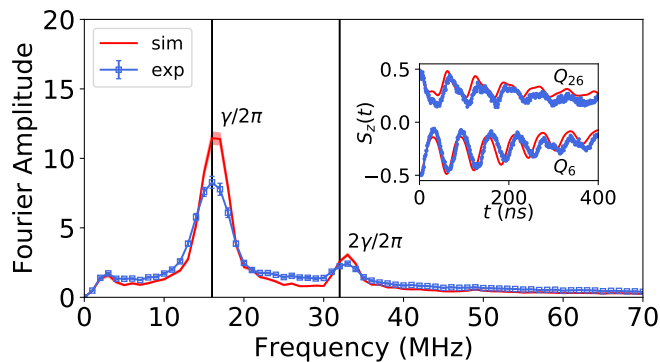


Figure 5. **Bloch oscillations in the Stark MBL phase.** Average Fourier amplitude of the real-time oscillations of $\langle \sigma_i^z \rangle$ for each qubit Q_i ; inset displays, for example, the dynamics of two qubits, Q_6 and Q_{26} . These are selected in order to (i) visualize the high amplitude of the oscillations, making the identification of periods more easily discernible, and (ii) amplify the signal to noise ratio; nonetheless, the Fourier amplitudes for the oscillations of *all* qubits are averaged in the main panel. Peaks at $\omega = \gamma/2\pi$ and higher harmonics, describe the Bloch oscillations with frequencies given by the Stark potential, explaining the mechanisms of emerging integrability in the MBL phase. In all data presented, averages and error bars stem from repetitions of a single product state initialization; markers (lines) denote experimental (numerical simulation) data.

and M. Zwierlein, Quantum simulators: Architectures and opportunities (2019), [arXiv:1912.06938 \[quant-ph\]](https://arxiv.org/abs/1912.06938).

- [3] I. M. Georgescu, S. Ashhab, and F. Nori, Quantum simulation, *Rev. Mod. Phys.* **86**, 153 (2014).
- [4] C. Neill, P. Roushan, K. Kechedzhi, S. Boixo, S. V. Isakov, V. Smelyanskiy, A. Megrant, B. Chiaro, A. Dunsworth, K. Arya, R. Barends, B. Burkett, Y. Chen, Z. Chen, A. Fowler, B. Foxen, M. Giustina, R. Graff, E. Jeffrey, T. Huang, J. Kelly, P. Klimov, E. Lucero, J. Mutus, M. Neeley, C. Quintana, D. Sank, A. Vainsencher, J. Wenner, T. C. White, H. Neven, and J. M. Martinis, A blueprint for demonstrating quantum supremacy with superconducting qubits, *Science* **360**, 195 (2018).
- [5] Post-K (Fugaku) information, <https://postk-web.r-ccs.riken.jp/spec.html>, accessed: 2020-11-14.
- [6] We estimate that under a perfect parallelization scenario, that is, with no overheads and bandwidth bottlenecks, the distributed diagonalization of such Hamiltonian would require approximately 295 years in the Fugaku supercomputer when using 32 qubits and over 7 months for $N = 29$.
- [7] J. M. Deutsch, Quantum statistical mechanics in a closed system, *Phys. Rev. A* **43**, 2046 (1991).
- [8] M. Srednicki, Chaos and quantum thermalization, *Phys. Rev. E* **50**, 888 (1994).
- [9] F. Haake, *Quantum Signatures of Chaos* (Springer-Verlag, Berlin, Heidelberg, 2006).
- [10] M. Rigol, V. Dunjko, and M. Olshanii, Thermalization and its mechanism for generic isolated quantum systems, *Nature* **452**, 854 (2008).
- [11] Y. K. L. D’Alessio, A. Polkovnikov, and M. Rigol, From quantum chaos and eigenstate thermalization to statistical mechanics and thermodynamics, *Advances in Physics* **65**, 239 (2016).
- [12] G. Clos, D. Porras, U. Warring, and T. Schaetz, Time-resolved observation of thermalization in an isolated quantum system, *Phys. Rev. Lett.* **117**, 170401 (2016).
- [13] C. Neill, P. Roushan, M. Fang, Y. Chen, M. Kolodrubetz, Z. Chen, A. Megrant, R. Barends, B. Campbell, B. Chiaro, A. Dunsworth, E. Jeffrey, J. Kelly, J. Mutus, P. J. J. O’Malley, C. Quintana, D. Sank, A. Vainsencher, J. Wenner, T. C. White, A. Polkovnikov, and J. M. Martinis, Ergodic dynamics and thermalization in an isolated quantum system, *Nature Physics* **12**, 1037 (2016).
- [14] A. M. Kaufman, M. E. Tai, A. Lukin, M. Rispoli, R. Schittko, P. M. Preiss, and M. Greiner, Quantum thermalization through entanglement in an isolated many-body system, *Science* **353**, 794 (2016).
- [15] R. Nandkishore and D. A. Huse, Many-body localization and thermalization in quantum statistical mechanics, *Annual Review of Condensed Matter Physics* **6**, 15 (2015).
- [16] E. Altman, Many-body localization and quantum thermalization, *Nature Physics* **14**, 979 (2018).
- [17] D. A. Abanin, E. Altman, I. Bloch, and M. Serbyn, Colloquium: Many-body localization, thermalization, and entanglement, *Rev. Mod. Phys.* **91**, 021001 (2019).
- [18] P. W. Anderson, Absence of diffusion in certain random lattices, *Phys. Rev.* **109**, 1492 (1958).
- [19] D. Basko, I. Aleiner, and B. Altshuler, Metal-insulator transition in a weakly interacting many-electron system with localized single-particle states, *Annals of Physics* **321**, 1126 (2006).

- [20] J. Z. Imbrie, Diagonalization and many-body localization for a disordered quantum spin chain, *Phys. Rev. Lett.* **117**, 027201 (2016).
- [21] M. Žnidarič, T. c. v. Prosen, and P. Prelovšek, Many-body localization in the Heisenberg XXZ magnet in a random field, *Phys. Rev. B* **77**, 064426 (2008).
- [22] A. Pal and D. A. Huse, Many-body localization phase transition, *Phys. Rev. B* **82**, 174411 (2010).
- [23] J. A. Kjäll, J. H. Bardarson, and F. Pollmann, Many-body localization in a disordered quantum Ising chain, *Phys. Rev. Lett.* **113**, 107204 (2014).
- [24] D. J. Luitz, N. Laflorencie, and F. Alet, Many-body localization edge in the random-field Heisenberg chain, *Phys. Rev. B* **91**, 081103 (2015).
- [25] R. Mondaini and M. Rigol, Many-body localization and thermalization in disordered Hubbard chains, *Phys. Rev. A* **92**, 041601 (2015).
- [26] M. Schreiber, S. S. Hodgman, P. Bordia, H. P. Lüschen, M. H. Fischer, R. Vosk, E. Altman, U. Schneider, and I. Bloch, Observation of many-body localization of interacting fermions in a quasirandom optical lattice, *Science* **349**, 842 (2015).
- [27] J.-y. Choi, S. Hild, J. Zeiher, P. Schauß, A. Rubio-Abadal, T. Yefsah, V. Khemani, D. A. Huse, I. Bloch, and C. Gross, Exploring the many-body localization transition in two dimensions, *Science* **352**, 1547 (2016).
- [28] J. Smith, A. Lee, P. Richerme, B. Neyenhuis, P. W. Hess, P. Hauke, M. Heyl, D. A. Huse, and C. Monroe, Many-body localization in a quantum simulator with programmable random disorder, *Nature Physics* **12**, 907 EP (2016).
- [29] H. P. Lüschen, P. Bordia, S. Scherg, F. Alet, E. Altman, U. Schneider, and I. Bloch, Observation of slow dynamics near the many-body localization transition in one-dimensional quasiperiodic systems, *Phys. Rev. Lett.* **119**, 260401 (2017).
- [30] P. Roushan, C. Neill, J. Tangpanitanon, V. M. Bastidas, A. Megrant, R. Barends, Y. Chen, Z. Chen, B. Chiaro, A. Dunsworth, A. Fowler, B. Foxen, M. Giustina, E. Jeffrey, J. Kelly, E. Lucero, J. Mutus, M. Neeley, C. Quintana, D. Sank, A. Vainsencher, J. Wenner, T. White, H. Neven, D. G. Angelakis, and J. Martinis, Spectroscopic signatures of localization with interacting photons in superconducting qubits, *Science* **358**, 1175 (2017).
- [31] K. Xu, J.-J. Chen, Y. Zeng, Y.-R. Zhang, C. Song, W. Liu, Q. Guo, P. Zhang, D. Xu, H. Deng, K. Huang, H. Wang, X. Zhu, D. Zheng, and H. Fan, Emulating many-body localization with a superconducting quantum processor, *Phys. Rev. Lett.* **120**, 050507 (2018).
- [32] K. X. Wei, C. Ramanathan, and P. Cappellaro, Exploring localization in nuclear spin chains, *Phys. Rev. Lett.* **120**, 070501 (2018).
- [33] T. Kohlert, S. Scherg, X. Li, H. P. Lüschen, S. Das Sarma, I. Bloch, and M. Aidelsburger, Observation of many-body localization in a one-dimensional system with a single-particle mobility edge, *Phys. Rev. Lett.* **122**, 170403 (2019).
- [34] M. Rispoli, A. Lukin, R. Schittko, S. Kim, M. E. Tai, J. Léonard, and M. Greiner, Quantum critical behaviour at the many-body localization transition, *Nature* **573**, 385 (2019).
- [35] Q. Guo, C. Cheng, Z.-H. Sun, Z. Song, H. Li, Z. Wang, W. Ren, H. Dong, D. Zheng, Y.-R. Zhang, R. Mondaini, H. Fan, and H. Wang, Observation of energy-resolved many-body localization, *Nature Physics* [10.1038/s41567-020-1035-1](https://doi.org/10.1038/s41567-020-1035-1) (2020).
- [36] T. Grover and M. P. A. Fisher, Quantum disentangled liquids, *J. Stat. Mech.: Theory and Experiment*, P10010 (2014).
- [37] N. Y. Yao, C. R. Laumann, J. I. Cirac, M. D. Lukin, and J. E. Moore, Quasi-many-body localization in translation-invariant systems, *Phys. Rev. Lett.* **117**, 240601 (2016).
- [38] A. Smith, J. Knolle, R. Moessner, and D. L. Kovrizhin, Absence of ergodicity without quenched disorder: From quantum disentangled liquids to many-body localization, *Phys. Rev. Lett.* **119**, 176601 (2017).
- [39] G. H. Wannier, Wave functions and effective hamiltonian for Bloch electrons in an electric field, *Phys. Rev.* **117**, 432 (1960).
- [40] G. H. Wannier, Dynamics of band electrons in electric and magnetic fields, *Rev. Mod. Phys.* **34**, 645 (1962).
- [41] M. Schulz, C. A. Hooley, R. Moessner, and F. Pollmann, Stark many-body localization, *Phys. Rev. Lett.* **122**, 040606 (2019).
- [42] E. van Nieuwenburg, Y. Baum, and G. Refael, From Bloch oscillations to many-body localization in clean interacting systems, *Proceedings of the National Academy of Sciences* **116**, 9269 (2019).
- [43] S. R. Taylor, M. Schulz, F. Pollmann, and R. Moessner, Experimental probes of Stark many-body localization, *Phys. Rev. B* **102**, 054206 (2020).
- [44] R. Yao and J. Zakrzewski, Many-body localization of bosons in an optical lattice: Dynamics in disorder-free potentials, *Phys. Rev. B* **102**, 104203 (2020).
- [45] P. Sala, T. Rakovszky, R. Verresen, M. Knap, and F. Pollmann, Ergodicity breaking arising from Hilbert space fragmentation in dipole-conserving Hamiltonians, *Phys. Rev. X* **10**, 011047 (2020).
- [46] F. Meinert, M. J. Mark, E. Kirilov, K. Lauber, P. Weinmann, M. Gröbner, and H.-C. Nägerl, Interaction-induced quantum phase revivals and evidence for the transition to the quantum chaotic regime in 1d atomic Bloch oscillations, *Phys. Rev. Lett.* **112**, 193003 (2014).
- [47] See Supplemental Material for more details.
- [48] C. Song, K. Xu, H. Li, Y.-R. Zhang, X. Zhang, W. Liu, Q. Guo, Z. Wang, W. Ren, J. Hao, H. Feng, H. Fan, D. Zheng, D.-W. Wang, H. Wang, and S.-Y. Zhu, Generation of multicomponent atomic Schrödinger cat states of up to 20 qubits, *Science* **365**, 574 (2019).
- [49] P. Hauke and M. Heyl, Many-body localization and quantum ergodicity in disordered long-range Ising models, *Phys. Rev. B* **92**, 134204 (2015).
- [50] J. Haegeman, J. I. Cirac, T. J. Osborne, I. Pižorn, H. Verschelde, and F. Verstraete, Time-dependent variational principle for quantum lattices, *Phys. Rev. Lett.* **107**, 070601 (2011).
- [51] M. Yang and S. R. White, Time-dependent variational principle with ancillary Krylov subspace, *Phys. Rev. B* **102**, 094315 (2020).
- [52] G. De Tomasi, S. Bera, J. H. Bardarson, and F. Pollmann, Quantum mutual information as a probe for many-body localization, *Phys. Rev. Lett.* **118**, 016804 (2017).
- [53] B. Villalonga and B. K. Clark, Characterizing the many-body localization transition through correlations (2020), [arXiv:2007.06586 \[cond-mat.dis-nn\]](https://arxiv.org/abs/2007.06586).
- [54] J. H. Bardarson, F. Pollmann, and J. E. Moore, Unbounded growth of entanglement in models of many-body

- localization, *Phys. Rev. Lett.* **109**, 017202 (2012).
- [55] M. Serbyn, Z. Papić, and D. A. Abanin, Universal slow growth of entanglement in interacting strongly disordered systems, *Phys. Rev. Lett.* **110**, 260601 (2013).
- [56] P. Ribeiro, A. Lazarides, and M. Haque, Many-body quantum dynamics of initially trapped systems due to a Stark potential: Thermalization versus Bloch oscillations, *Phys. Rev. Lett.* **124**, 110603 (2020).
- [57] E. Guardado-Sanchez, A. Morningstar, B. M. Spar, P. T. Brown, D. A. Huse, and W. S. Bakr, Subdiffusion and heat transport in a tilted two-dimensional Fermi-Hubbard system, *Phys. Rev. X* **10**, 011042 (2020).
- [58] V. Khemani, M. Hermele, and R. Nandkishore, Localization from Hilbert space shattering: From theory to physical realizations, *Phys. Rev. B* **101**, 174204 (2020).
- [59] S. Moudgalya, A. Prem, R. Nandkishore, N. Regnault, and B. A. Bernevig, Thermalization and its absence within Krylov subspaces of a constrained Hamiltonian (2019), [arXiv:1910.14048 \[cond-mat.str-el\]](https://arxiv.org/abs/1910.14048).
- [60] N. Macé, F. Alet, and N. Laflorencie, Multifractal scalings across the many-body localization transition, *Phys. Rev. Lett.* **123**, 180601 (2019).
- [61] S. Scherg, T. Kohlert, P. Sala, F. Pollmann, B. H. M., I. Bloch, and M. Aidelsburger, Observing non-ergodicity due to kinetic constraints in tilted Fermi-Hubbard chains (2020), [arXiv:2010.12965 \[cond-mat.quant-gas\]](https://arxiv.org/abs/2010.12965).
- [62] Z. Chen, A. Megrant, J. Kelly, R. Barends, J. Bochmann, Y. Chen, B. Chiaro, A. Dunsworth, E. Jeffrey, J. Y. Mutus, P. J. J. O'Malley, C. Neill, P. Roushan, D. Sank, A. Vainsencher, J. Wenner, T. C. White, A. N. Cleland, and J. M. Martinis, Fabrication and characterization of aluminum airbridges for superconducting microwave circuits, *Applied Physics Letters* **104**, 052602 (2014).
- [63] Y. Y. Atas, E. Bogomolny, O. Giraud, and G. Roux, Distribution of the ratio of consecutive level spacings in random matrix ensembles, *Phys. Rev. Lett.* **110**, 084101 (2013).
- [64] W. Beugeling, R. Moessner, and M. Haque, Finite-size scaling of eigenstate thermalization, *Phys. Rev. E* **89**, 042112 (2014).

Supplementary Materials: Stark many-body localization on a superconducting quantum processor

This supplementary information describes the experimental device, as its fabrication, engineered qubit couplings, as well as provides supporting information of the ergodicity breakdown via exact numerical calculations on a smaller number of qubits, and other numerical relevant details, as benchmarks of the TDVP method.

CONTENTS

References	5
Device fabrication	9
Device Characterization	9
The physical model for numerics	9
Measurements of Qubit Couplings	10
Synchronization of Z pulses via bus resonator	11
Dynamics of two-body correlations	11
Numerical details	11
Initial state average	12
ETH analysis and the emerging dipole conservation	12

DEVICE FABRICATION

This 32-qubit device was fabricated using the recipe including the following four steps:

1. Aluminum deposition. 100 nm Al layer is deposited on a 330 μm one-side polished sapphire substrate using electron beam evaporation.
2. Etching basic circuitry. A layer of photoresist (SPR955 7.0) is spin coated on top of the Al layer. Then, patterns for basic circuitry including qubit capacitors, ground plane, readout resonators, control wires, and bus resonator are defined using a direct-write laser system (DWL66+), which are translated to the Al layer by development and subsequent wet-etching (etchant: 2.38% TMAH).
3. Josephson junction deposition and lift-off. Double layers of 500 nm copolymer and 300 nm PMMA are used to define the junction area with electron beam lithography (50 kV), followed by development

in the MIBK/IPA (1:3) solution. The Al-AlO_x-Al Josephson junctions are then deposited using the double-angle electron beam evaporation.

4. Fabrication of aluminum airbridges. This step is similar to that in Ref. [62]

DEVICE CHARACTERIZATION

The device [Fig. 1(A)] used in this work consists of 32 transmon qubits, and a central bus resonator \mathcal{R} . The typical circuit structure for a qubit, as shown in Fig. S1, is composed of a capacitor, a superconducting quantum interference device (SQUID) and the additional quantum control circuitry, including a Z line for tuning qubit frequency, an XY line for exciting qubit $|0\rangle \leftrightarrow |1\rangle$ transition, and a capacitively coupled $\lambda/4$ coplanar waveguide resonator for dispersive readout. The typical qubit lifetimes are $\sim 23 \mu\text{s}$ for the relaxation time T_1 and $\sim 0.9 \mu\text{s}$ for the Ramsey dephasing time, both of which vary depending on the qubit frequency. We note that the true timescales describing the dephasing effects for an *interacting* many-body system, actively coupled, are in practice much longer than the single-qubit Ramsey dephasing times, as has been reported in our previous work using an analogous device [35]. The detailed information on qubits' performance is collected in Tab. S1. The experimental setup for qubit control and readout can be found in Ref. [48].

THE PHYSICAL MODEL FOR NUMERICS

In this device, the connectivity J_{ij} , in equation (1) of the main text, is provided by both the central bus \mathcal{R} mediated interactions and the capacitance induced direct couplings. The former are reasonably small due to the large detunings between the bus frequency (~ 7 GHz) and the qubits' interaction frequencies (around 5.15 GHz), so that the capacitance induced direct couplings dominate the system's dynamics. The physical model emulated in the experiment is extracted by systematically measuring the dominant J_{ij} terms, which is used as an input for numerical simulations.

At the current stage, three qubits do not function properly, thus, in this work, we use 29 qubits for emulating Stark many-body localization. The coupling topology is shown in Fig. S2(A). By using the displayed coupling values, numerical simulations are carried out to benchmark the experiment. Note that qubit indices have been relabeled from Q_1 to Q_{29} , from right to left, for the selected

	$\omega_{j,\text{idle}}/2\pi$ (GHz)	$T_{1j,\text{idle}}$ (μs)	\bar{T}_{1j} (μs)	$\omega_{r,j}/2\pi$ (μs)	$F_{0,j}$ (MHz)	$F_{1,j}$ (GHz)
Q_1	5.529	~ 27	~ 29	6.571	0.972	0.914
Q_2	4.260	~ 39	~ 21	6.550	0.929	0.896
Q_3	5.060	~ 19	~ 26	6.600	0.981	0.915
Q_4	4.159	~ 57	~ 29	6.533	0.940	0.909
Q_5	5.681	~ 16	~ 28	6.612	0.970	0.906
Q_6	4.083	~ 42	~ 21	6.504	0.957	0.916
Q_7	4.761	~ 34	~ 29	6.651	0.975	0.941
Q_8	4.294	~ 23	~ 18	6.478	0.962	0.918
Q_9	4.857	~ 27	~ 27	6.466	0.957	0.921
Q_{10}	5.564	~ 17	~ 21	6.721	0.964	0.851
Q_{11}	5.423	~ 20	~ 26	6.444	0.936	0.904
Q_{12}	-	-	-	6.647	-	-
Q_{13}	4.929	~ 21	~ 23	6.439	0.969	0.915
Q_{14}	4.130	~ 40	~ 24	6.608	0.942	0.888
Q_{15}	4.340	~ 37	~ 28	6.431	0.947	0.910
Q_{16}	5.040	~ 24	~ 20	6.543	0.958	0.900
Q_{17}	4.229	~ 60	~ 22	6.525	0.931	0.907
Q_{18}	5.720	~ 9	~ 31	6.469	0.945	0.869
Q_{19}	5.599	~ 25	~ 22	6.531	0.942	0.919
Q_{20}	4.959	~ 16	~ 21	6.529	0.964	0.932
Q_{21}	3.997	~ 34	~ 21	6.512	0.963	0.931
Q_{22}	4.902	~ 29	~ 22	6.594	0.954	0.892
Q_{23}	-	-	~ 22	6.528	-	-
Q_{24}	5.453	~ 29	~ 21	6.650	0.961	0.900
Q_{25}	4.733	~ 28	~ 24	6.708	0.951	0.920
Q_{26}	4.050	~ 28	~ 18	6.393	0.935	0.912
Q_{27}	4.830	~ 31	~ 25	6.661	0.919	0.889
Q_{28}	5.635	~ 15	~ 28	6.439	0.951	0.872
Q_{29}	-	-	~ 22	6.597	-	-
Q_{30}	4.213	~ 30	~ 6	6.488	0.903	0.888
Q_{31}	4.801	~ 35	~ 19	6.568	0.931	0.904
Q_{32}	5.497	~ 22	~ 24	6.537	0.959	0.890

Table S1. **Typical device performance.** $\omega_{j,\text{idle}}$ is the Q_j 's idle frequency, where the initial states are prepared. Q_{12} , Q_{23} , Q_{29} are not used, which are placed around their sweet points (> 6.5 GHz) during the whole experiment. The energy relaxation time of Q_j at its idle frequency is denoted as $T_{1j,\text{idle}}$. $\bar{T}_{1j,\text{operation}}$ describes the averaged energy relaxation time from 5.0 GHz to 5.3 GHz, where qubits interacting with each other for emulating Stark many-body localization physics for different linear potentials. $\omega_{r,j}$ is the resonant frequency of Q_j 's readout resonator (R_j). The readout fidelities are characterized by the measured probability for state $|0\rangle$ ($|1\rangle$), labeled as $F_{0,j}$ ($F_{1,j}$), when Q_j is prepared in state $|0\rangle$ ($|1\rangle$).

qubits in Fig S2(A). Figure S2(B) shows the coupling topology of 16 qubits, presenting an integrable model, used to quantify Wannier-Stark localization in the main text.

MEASUREMENTS OF QUBIT COUPLINGS

To extract the effective physical model emulated in this experiment, J_{ij} is carefully calibrated by measuring Q_i - Q_j 's on-resonance energy swap dynamics at the

frequency around 5.15 GHz, the center of the operation frequencies of the 29 qubits. The related pulse sequence is shown in Fig. S3(A), in which Q_i and Q_j are prepared to $|10\rangle$ and then, two square pulses are applied simultaneously to tune their frequencies to ~ 5.15 GHz, with Q_j 's frequency being varied. After an interaction time t , both qubits are jointly measured to record P_{10} versus t . For example, Fig. S3(B) shows the experimental data for calibrating the coupling strength between Q_{10} and Q_8 . When the two qubits are on resonance, the oscillation of P_{10} versus t reaches a minimum in frequency, which is

twice of the coupling strength $J_{ij}/2\pi$. The corresponding fitting results are shown in Fig. S3(C), where the minimum point (orange) indicates a coupling strength of 3.5 MHz for Q_{10} and Q_8 .

SYNCHRONIZATION OF Z PULSES VIA BUS RESONATOR

For the device with only nearest-neighbor connectivity, the timing offsets between the control lines of different qubits are calibrated by selecting a reference qubit and measuring the relative offsets of the neighboring qubits. The process is done consecutively until all qubits are covered. The issue is that the calibration errors tend to propagate and accumulate as the number of qubits increases. In our device, the central bus resonator could be tuned in frequency to interact with the qubits, providing an optimal medium to calibrate such timing offsets between any pair of qubits directly, which could minimize the accumulation of errors.

The pulse sequence for calibrating the Z pulse timing offset between the qubit pair $\{Q_i, Q_j\}$ is shown in Fig. S4(A). Q_i is excited to $|1\rangle$ with a π pulse and then two square pulses separated by a time delay τ for swapping the photon between the bus resonator \mathcal{R} and Q_i are applied. At the same time, a square pulse with a length of τ for swapping the photon between \mathcal{R} and Q_j is applied, whose start time varies with a delay of Δt relative to the first square pulse on Q_i . If Q_j 's square pulse is right in-between the two square pulses on Q_i , signals through the Z control lines of Q_i and Q_j are well synchronized. The representative experimental data for a well synchronized qubit pair are shown in Fig. S4(B), which calibrates the Z pulse timing between the far separated Q_{31} and Q_1 .

DYNAMICS OF TWO-BODY CORRELATIONS

One of the main characteristics of quantum many-body systems in out-of-equilibrium is the presence of large entanglement among its constituents. As we have argued in the main text, this can be inferred by the large degree of correlations between physically distant qubits, and owing the null-entangled initial product state, global entanglement builds up over the course of the dynamics. To better understand this evolution, we show in Fig. S5 snapshots of the experimentally measured two-body correlations, further contrasting it with growing Stark potentials. Under the ergodic regime, $\gamma/2\pi = 1$ MHz, the correlations quickly grow at very early times, in particular, for $t = 45$ ns (around one tunneling time $\propto 1/J_{ij}$), they extend already beyond nearest-neighbor qubits. Equilibration is already seen at $t = 500$ ns, with $C(i, j)$'s spread over all qubit pairs, in similarity to the results at the largest experimental time $t = 1000$ ns.

For larger tilt potentials ($\gamma/2\pi = 5$ and 8 MHz), the build-up of correlations at early times for nearest-neighbors similarly occurs, however, it quickly gets ‘frozen’ in this regime, with no significant growth past this short-ranged scale within experimentally accessible times. This marks the non-ergodic behavior outlined in the main text, due to the presence of the nonrandom potential.

NUMERICAL DETAILS

We focus on the dynamics at the middle of the eigen-spectrum, thus one needs knowledge of the maximum and minimum energies in advance in order to select initial states (which univocally define the system’s total energy) as to probe this region of the spectrum. In practice, the two extremal states are calculated by solving the ground state of H and $-H$, via the density matrix renormalization group (DMRG) method. In this, we perform 10 DMRG sweeps to obtain a highly accurate target state, with truncation error smaller than 10^{-12} .

To benchmark the real-time dynamics with experimental results, we adopted the time-dependent variational principle (TDVP) algorithm in finite matrix product states (MPSs) [50]. By projecting the time-dependent Schrödinger equation to the tangent space of the MPS manifold at each time step, this method is able to handle real-time dynamics of the system with long-ranged terms. However, for the evolution starting from a product state, which is a MPS of bond dimension one with a limited tangent space, both one-site and two-site TDVP methods may fail to capture the true direction of motion. In our calculations, we take the global subspace expansion procedure [51] in the first 20 time steps to enlarge the tangent space of the low entangled state. As to balance accuracy and computational complexity, we use more-expensive two-site TDVP algorithms in the first 100 time steps, and one-site sweeps in the subsequent ones, when the tangent space contains sufficient degree of freedom. For the same reason, various discrete time steps are selected from 2 to 5 nanoseconds, for different γ 's. The maximum bond dimension is 3000 for all calculations in the main text; and the truncation error is always smaller than 10^{-4} .

When using a smaller number of qubits ($N = 20$), with the experimentally relevant parameters, we have further benchmarked the evolution obtained via TDVP with the exact results of the unitary evolution (Fig. S6) within the experimental pertinent times. The agreement, either for small or large tilt potentials γ is remarkable. Now, fully resorting to the total number of qubits experimentally employed ($N = 29$), we further test the convergence of the TDVP results by systematically enlarging the bond-dimension χ (Fig. S7), at the most challenging regime of the parameter space, i.e., when γ is small,

and large entanglement is still manifest (See Fig. 3 in the main text). Again the unitary dynamics does not present quantitatively relevant discrepancies, attesting the usage of $\chi = 3000$ as a sufficient bond dimension in this demanding scenario.

INITIAL STATE AVERAGE

For a system without explicit disorder, the standard procedure of averaging observed quantities over an ensemble of disorder realizations is no longer applicable. On top of usual measurement repetitions for a given initial state, we employ a second scheme that increases the overall statistics of the presented data. To start, we numerically obtain the spectrum of all product states, that is, $E^{(n)} = \langle \Psi_0^{(n)} | H | \Psi_0^{(n)} \rangle$ with a given conserved number of photon excitations, for a given γ potential. Then, after using the previously explained scheme for numerically extracting the ground state energy E_{GS} of H and its highest excited state E_{max} , we are able to locate the product state energies in the eigenenergy density spectrum of the Hamiltonian.

We thus proceed by randomly selecting 20 initial product states within a narrow energy density window $\varepsilon_{\text{target}} = 0.5 \pm 0.02$. To understand how unrelated are these 20 initial states, we compute the standard Hamming distance \mathcal{HD} (a measure of how different are two bitstrings representing the product states by counting the number of different bits, and not a dynamical observable as used in the main text) between each pair of states in this subset. Histograms of the \mathcal{HD} for the initial states used are presented in Fig. S8, over a large range of tilt potentials. The histogram profiles are essentially Gaussian within this approach, and allow one to use this procedure to promote statistical averages of the quantities in the main text.

ETH ANALYSIS AND THE EMERGING DIPOLE CONSERVATION

To better understand the onset of non-ergodic behavior with growing tilt potential γ , we will now make use of typical ETH expectations, accompanied by quantum chaotic predictions on the level repulsion of eigenenergies E_α of H . For that, we will restrict the numerical analysis, to up to 18 qubits, in order to make it amenable to exact diagonalization methods, while keeping the experimentally relevant parameters. When promoting such system size analysis, the choice of qubits is made such as to denote the smallest ‘volume’ in the corresponding lattice.

With increasing Stark potential, the Hilbert space fragments in subspaces, where the dipole-moment emerges as a conserved quantity in the limit $\gamma \rightarrow \infty$. To

test this, we show in Fig. S9 the eigenstate expectation values (EEV) of the dipole moment operator $\hat{d} \equiv \sum_j j \hat{n}_j$, when selecting 16 qubits. At small γ values, the expectation values display characteristic features of a thermalizing system, featuring a smooth variation with the energy, and exponentially small fluctuations in the system size (See Fig. S10 for a quantitative analysis). Directly related to the quantum chaotic predictions, the distribution of the ratio of adjacent gaps $r_\alpha = \min(\delta_\alpha, \delta_{\alpha+1}) / \max(\delta_\alpha, \delta_{\alpha+1})$, with consecutive gaps $\delta_\alpha \equiv E_{\alpha+1} - E_\alpha$ in the ordered list of eigenenergies $\{E_\alpha\}$, follows the corresponding random matrix ensemble expectation (Gaussian orthogonal ensemble - GOE): $P_{\text{GOE}}(r) = \frac{27}{8} \frac{r+r^2}{(1+r+r^2)^{\frac{5}{2}}}$ [63], at $\gamma \lesssim \bar{J}$. Larger

Stark potentials, on the other hand, remove the characteristic level repulsion and a Poisson distribution $P_{\text{P}}(r) = 2/(1+r)^2$ ensues, preceding the appearance of primordial fragmentation. For $\gamma \gg \bar{J}$, full fragmentation develops, where each eigenstate subspace is separated by approximately γ , and is characterized by an *integer* dipole-moment quantum number. We further contrast these results with a standard MBL scenario [See Figs. S9(I) and (J)], where we randomly set the onsite energy landscape from a uniform distribution. In this case, level repulsion is similarly absent, but dipole-moment is no longer a conserved quantity.

A quantitative analysis of the validity of the ETH can be made by the scaling form of the average value of the eigenstate-to-eigenstate fluctuations with growing dimension of the Hilbert space [11]. For that, we compute the absolute difference of EEVs in consecutive eigenstates, $\Delta\mathcal{O} \equiv |\langle \alpha | \hat{\mathcal{O}} | \alpha \rangle - \langle \alpha + 1 | \hat{\mathcal{O}} | \alpha + 1 \rangle|$, which provides an estimation of the fluctuations for a generic few-body operator $\hat{\mathcal{O}}$. Due to the extensive nature of the the dipole-moment operator, we analyze its normalized version, $(1/N^2)\hat{d}$, in Fig. S10.

It has been shown for non-integrable models satisfying the ETH, that such fluctuations decay as a power-law of the Hilbert space dimension, \mathcal{N}^a , with $a = -1/2$ if sufficiently far from their integrable points [64]. We test the scaling exponent for a range of values of the tilt potential in Fig. S10(B), restricting it to the regime before fragmentation takes place [See Fig. S9(C)]. At small tilt-potentials, the scaling exponents are slightly above $-1/2$, which we attribute to the finite-size effects that can affect the scaling, even more due the absence of perfect homogeneity of the device. Nevertheless, the approach to zero with increasing γ is a direct signature of the non-ergodic behavior, marking the breakdown of ETH. Moreover, if one instead repeats this analysis by selecting the more standard generalized imbalance (see main text) as the few-body operator under study, we notice similar characteristics for the departure of the ETH predictions [Fig. S10(B), ruling out the particularity of choosing an observable related to the emerging integrability at large

γ 's.

Now, since the standard experimental characterization of Stark MBL is performed via the quench dynamics of initial product states, one needs a metric to quantify how many eigenstates effectively contribute to the evolution of few-body observables. This can be readily obtained by numerically computing the width in energy associated to the initial state in the eigenenergy basis $\sigma(E) \equiv [\langle H^2 \rangle - \langle H \rangle^2]^{\frac{1}{2}} = [\sum_{\alpha} |\langle \Psi_0 | \alpha \rangle|^2 (E_{\alpha} - E)^2]^{\frac{1}{2}}$, for the energy conserving unitary evolution $E = \langle \Psi_0 | H | \Psi_0 \rangle = \langle \Psi_t | H | \Psi_t \rangle$. It is a time-independent quantity, reflecting the relevant Hilbert space spanned over the course of the dynamics.

Figure S11(A) presents the energy (density) resolved overlaps $|C_{\alpha}|^2 \equiv |\langle \Psi_0 | \alpha \rangle|^2$ for a large range of tilt potentials, when taking $|\Psi_0\rangle$ as an initial product state residing in the center of the eigenspectrum. As γ increases, and fragmentation takes place at $\gamma/2\pi \simeq 10$ MHz, a fairly small subset of eigenstate energies possess significant contribution on the overlaps, unlike in the ergodic regime at $\gamma \simeq \bar{J}$. This is the regime where one expects well developed Bloch oscillations as we experimentally demonstrate occurring at $\gamma/2\pi = 16$ MHz in the main text. Nonethe-

less, we have also argued there that smaller Stark potentials are already sufficient to induce the breakdown of ergodicity, being signified by either local-memory persistence over the course of the dynamics or the presence of slow (logarithm-in-time) growth of entanglement. However, according to the quantum chaos predictions [11, 63], non-ergodic behavior is directly inferred by energy level correlation (repulsion or its absence), and can be quantified by the average value of the ratio of adjacent gaps, \bar{r}_{ε} , taken within small energy windows .

Figure S11(B) displays a similar ‘phase diagram’ of \bar{r}_{ε} in the $\gamma - \varepsilon$ parameter space. At small γ 's, ergodic behavior is largely manifest, with ratio of adjacent gaps admitting values close to the GOE average $\bar{r}_{\text{GOE}} = 4 - 2\sqrt{3} \approx 0.5359$. On the other hand, much before the onset of fragmentation, energy levels start to become uncorrelated at $\gamma/2\pi \simeq 5$ MHz, and as a result, $\bar{r}_{\varepsilon} \rightarrow \bar{r}_{\text{P}} \approx 0.3862$. This goes in line with estimations of the onset of Stark MBL in the main text, although here using a much smaller Hilbert space, in order to make the extraction of exact eigenpairs amenable.

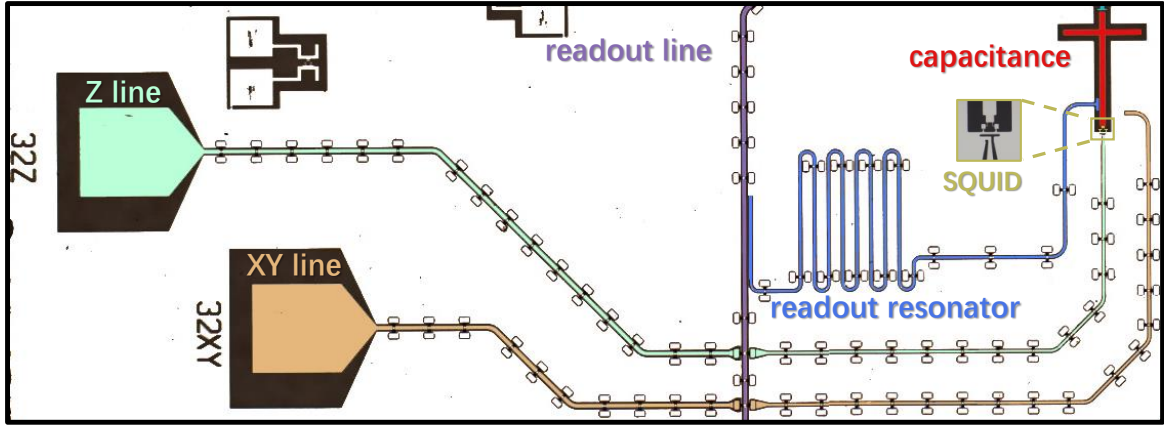


Figure S1. Micrograph showing the typical structure of a superconducting qubit. The qubit is a nonlinear oscillator consisting of a SQUID (yellow region with zoomed-in view in inset), which provides nonlinearity ($\omega_{21}/2\pi - \omega_{10}/2\pi \sim -0.33$ GHz) and frequency tunability, and a planar capacitor (red cross). The controllability is provided with a Z line (cyan), where we supply bias currents to tune qubit frequency and an XY line (brown) for applying microwave pulses to excite $|0\rangle \leftrightarrow |1\rangle$ transition. Qubit state measurements are implemented by detecting the dispersion of the probe signal through the readout line (purple), which is inductively coupled to a $\lambda/4$ superconducting resonator (blue) whose resonant frequency is qubit state-dependent. In this chip, there are 32 similar qubit modules like this. In order to suppress parasitic modes, different ground planes separated by coplanar waveguides are connected using air-bridges.

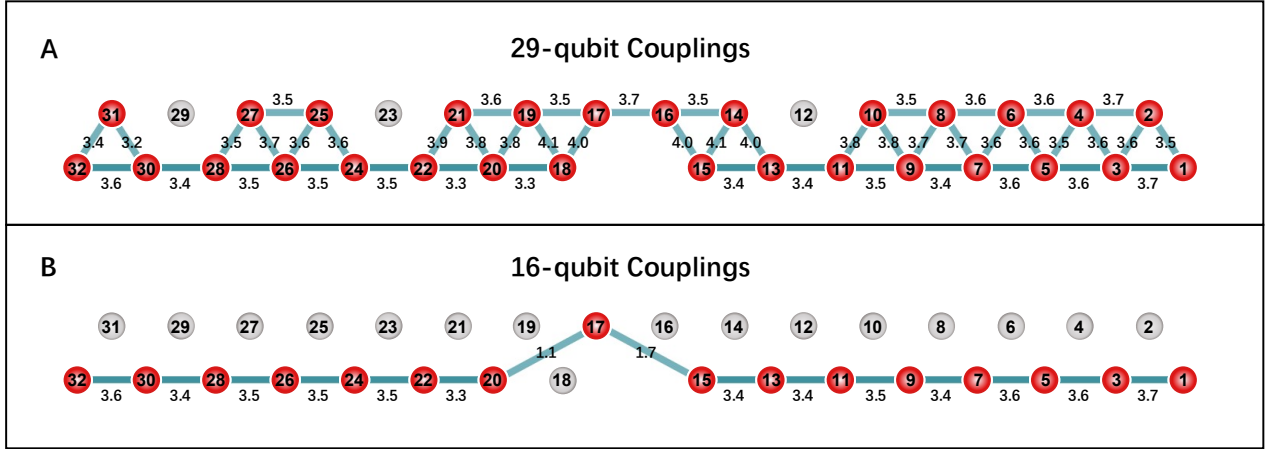


Figure S2. **Coupling topology used for numerical simulations.** (A) The coupling map of the 29 qubits for emulating Stark many-body localization. Red balls with numbers denote the qubits, and cyan lines connecting the balls represent the qubit couplings, with the coupling strengths $J_{ij}/2\pi$ listed. (B) The coupling map describing the effective linear chain of 16 qubits used in characterizing non-interacting localization (See Fig. 4 of the main text).

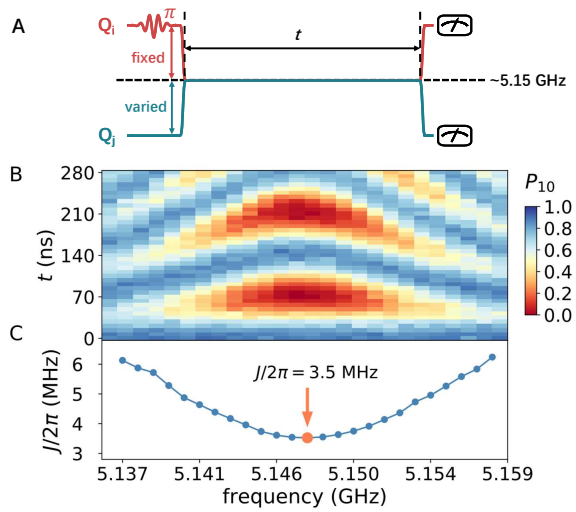


Figure S3. **Measurement of the qubit couplings.** (A) Pulse sequence for calibrating the coupling strength J_{ij} between Q_i and Q_j . (B) Experimentally measured swap dynamics for calibrating the coupling strength between Q_{10} and Q_8 . (C) Fitting results using the experimental data in panel (B), where the orange dot indicates the resonant interaction point, with a coupling strength of 3.5 MHz.

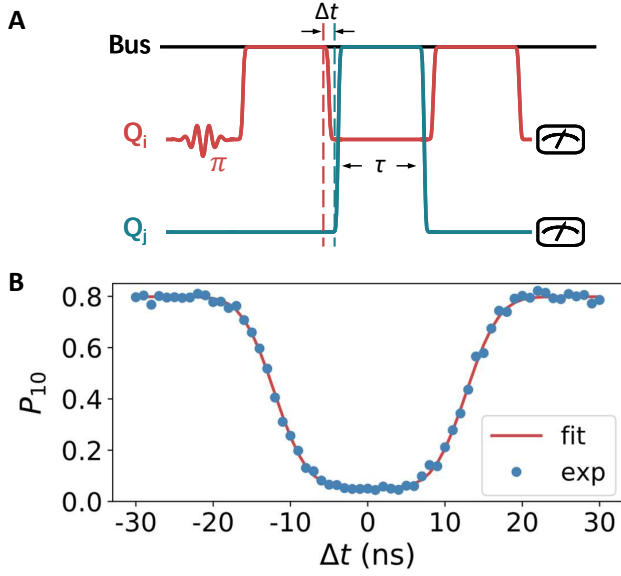


Figure S4. **Z pulse timing via the bus resonator.** (A) Pulse sequence used to calibrate the Z pulse timing between Q_i and Q_j . By varying the delay Δt , the two Z control lines for the qubit pair $\{Q_i, Q_j\}$ can be synchronized. When the relative delay Δt is small, the microwave photon in Q_i excited with its π pulse will be swapped to Q_j at the end of the sequence, yielding a small value of the measured probability in Q_i . In contrast, when $|\Delta t|$ is noticeable, Q_i 's photon will be swapped into the bus resonator and then back, with Q_i 's excitation remaining significant. (B) Experimental data for a synchronized qubit pair $\{Q_{31}, Q_1\}$. Blue dots are experimentally measured probability P_{10} using the pulse sequence in A. The center of the well shape determines the timing offset Δt .

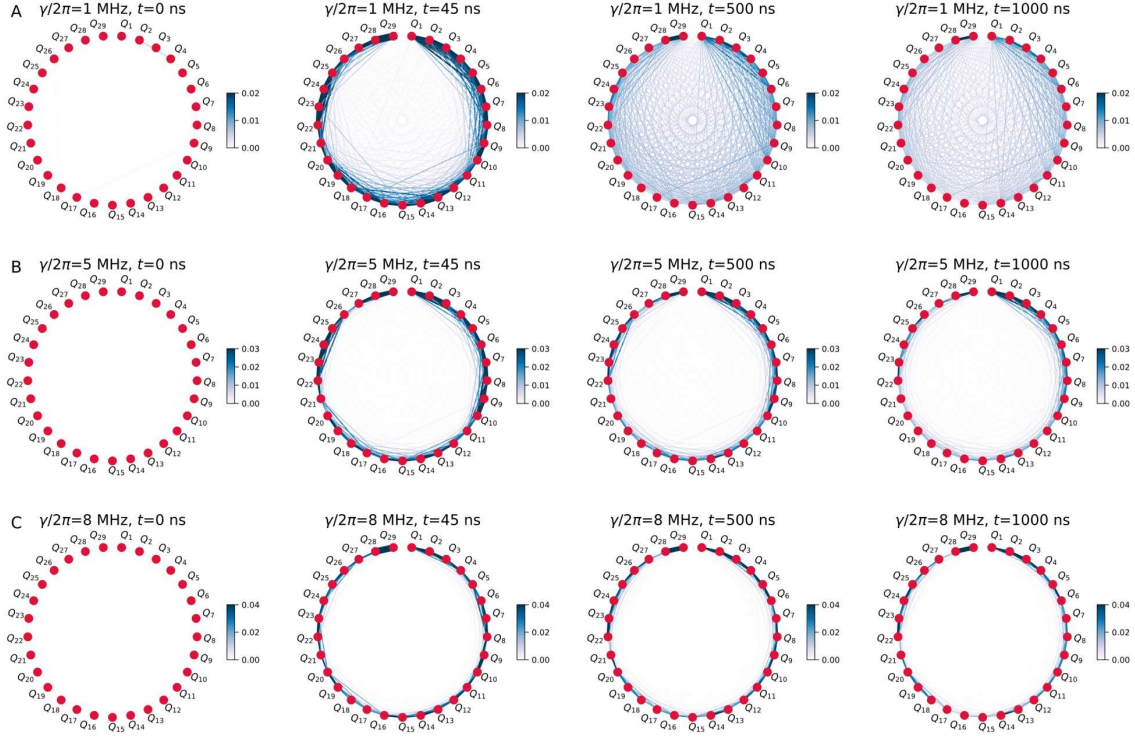


Figure S5. **Dynamics of two-body correlations.** Snapshots of the experimentally extracted two-body correlations $C(i, j)$ for $\gamma/2\pi = 1$ (A), 5 (B), and 8 MHz (C), from the initial time $t = 0$, where the product state is initialized, to the largest experimental time, $t = 1000$ ns. A small Stark potential is not sufficient to prevent the build-up of correlations across the device, resulting in a largely entangled evolved state at long times. On the other hand, $\gamma/2\pi = 5$ or 8 MHz, show the onset of non-ergodicity, where correlations are short-ranged with marginal growth within the experimentally accessible times.

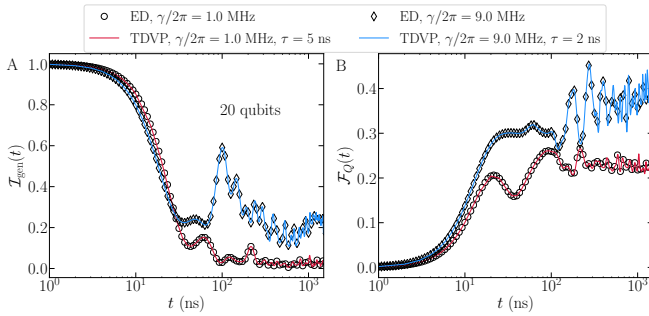


Figure S6. **TDVP benchmark against exact diagonalization (ED) results.** Numerically computed time-dependence of the generalized imbalance (A), and of the quantum Fisher information (B), when selecting 20 qubits of the device, preserving the experimentally relevant parameters. Markers (continuous lines) depict the ED (TDVP) results at small tilt potential $\gamma/2\pi = 1$ MHz or large one $\gamma/2\pi = 8$ MHz. In both cases, within the experimentally relevant times, the agreement between the different numerical methods is remarkable, and the evolution is studied from a single initial product state.

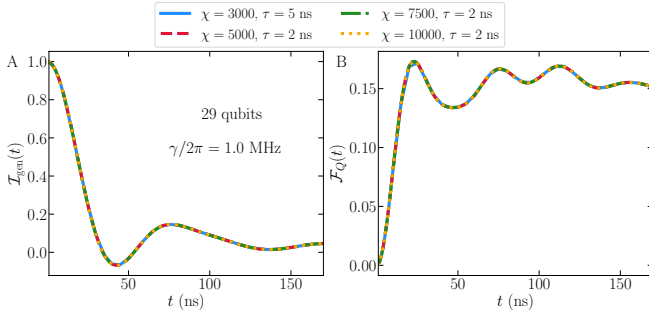


Figure S7. **Convergence of the TDVP evolution with bond-dimension χ .** We systematically test the convergence of the dynamics within the TDVP numerical approach by computing the time-dependence of the generalized imbalance (**A**), and of the quantum Fisher information (**B**), when tracking all of the $N = 29$ qubits experimentally used. Data is presented at the regime of largely ergodic behavior $\gamma/2\pi = 1$ MHz (and much smaller than the average coupling $\overline{J_{ij}}$). Up until close to the fast equilibration times, dynamics for all bond-dimensions χ is yet indiscernible. As with the ED benchmark, we study the evolution based on a single initial product state.

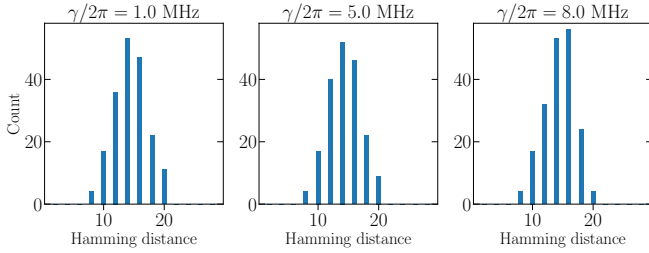


Figure S8. **Distribution of Hamming distances between pairs of initial states.** In order to promote statistical average with a deterministic potential, we average the extracted observables over 20 initial product states for each value of γ , whose energies lie in the center of the eigenspectrum of H . Their mutual Hamming distance is computed for $\gamma/2\pi = 1$ (left), 5 (center) and 8 MHz (right), and display an overall Gaussian profile; the same set of states is used in both experiments and numerical data.

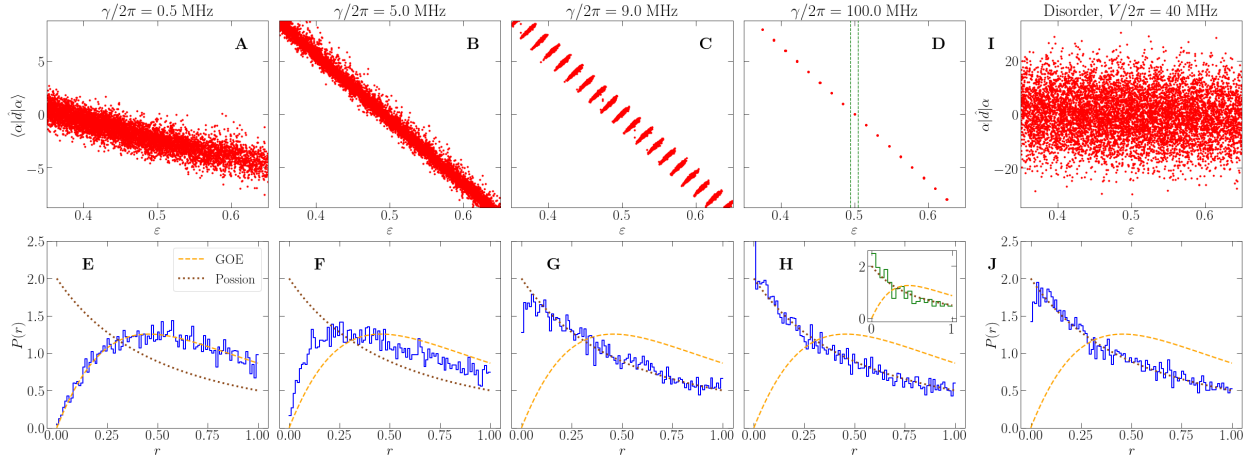


Figure S9. **EEV's and ratio of adjacent gaps.** (A)–(D) Numerically extracted eigenstate expectation values of the dipolar operator $\sum_j j \hat{n}_j$ close to the center of the spectrum ($\varepsilon = 0.5$) on a 16-qubit version of the device, with increasing potential γ as indicated. To facilitate visualization with the growing spectrum width as the Stark term is varied, we re-scale the eigenenergies E_α by plotting the energy density $\varepsilon = (E_\alpha - E_{\text{GS}})/(E_{\text{max}} - E_{\text{GS}})$ instead, where E_{GS} is the Hamiltonian's ground state, and E_{max} , its largest eigenenergy. (E)–(H) Distribution of the ratio of adjacent gaps r corresponding to the same tilt potentials as in (A)–(D). As a direct comparison, (I) and (J) display the corresponding $\langle \alpha | \hat{d} | \alpha \rangle$ and $P(r)$ if instead the energy landscape $\{W_j\}$ is randomly selected from a uniform distribution $W_j \in [-V, V]$, as in a typical MBL process. Level repulsion is similarly lost, but dipole-moment conservation is no longer present. The dashed lines in (D) limit the energies of the fragment with zero dipole moment, and whose ratio of adjacent gaps is analyzed in the inset of (H): again, level repulsion that is not manifested over the whole spectrum, is still absent within each fragmented subspace.

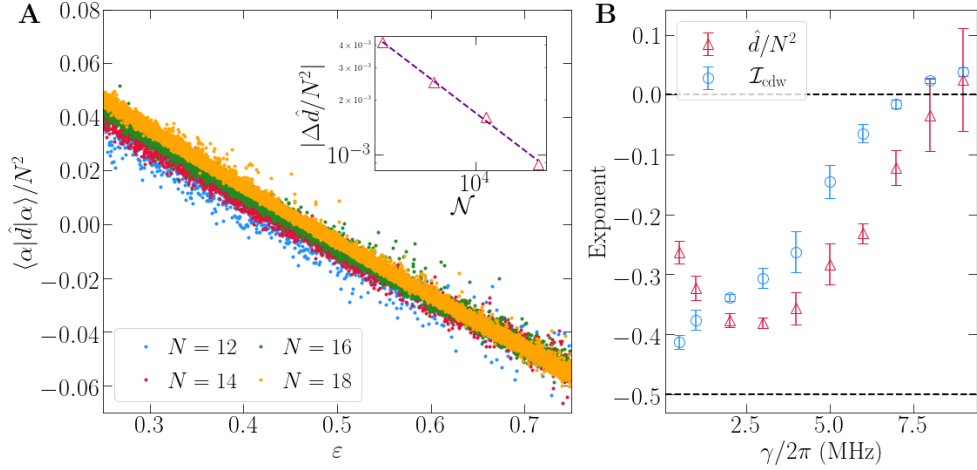


Figure S10. **The fluctuations of consecutive EEV's.** (A) The EEV's of the normalized dipole-operator $(1/N^2)\hat{d}$ for different system sizes, ranging from $N = 12$ to 18 qubits at $\gamma/2\pi = 2$ MHz; inset displays the corresponding scaling of the fluctuations with the Hilbert size dimension for the data set in the main panel. (B) The dependence of the scaling exponent of the EEV fluctuations on the tilt potential slope, obtained for both the normalized dipole and the standard charge-density wave imbalance operator $\hat{\mathcal{I}}$. The ETH predicted value, and its complete breakdown, are marked by the horizontal dashed lines at -0.5 and 0, respectively. Error bars stem from fitting uncertainties.

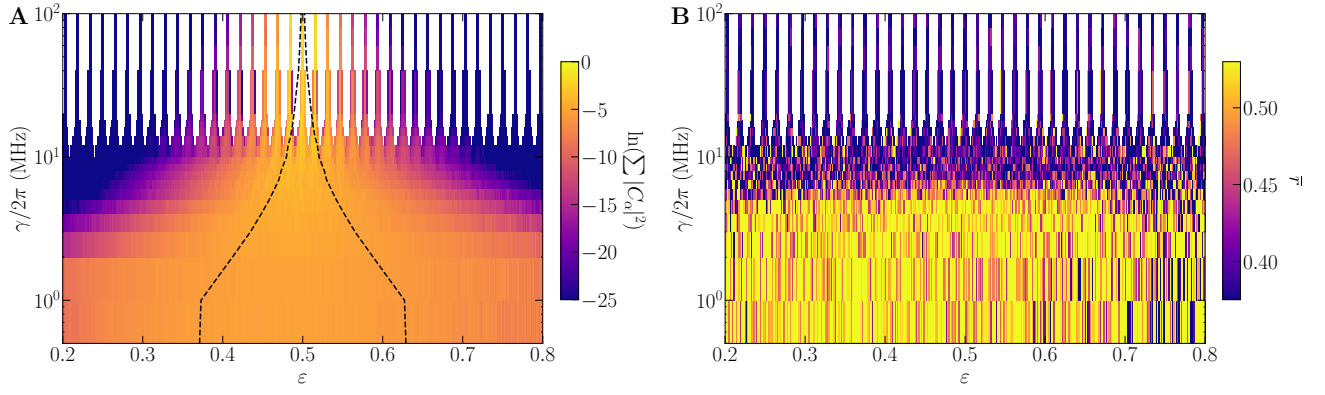


Figure S11. **The γ vs ε numerical phase diagram for 16-qubits.** (A) Color profile depicts the logarithm of the sum of probabilities $|C_\alpha|^2$ within each eigenenergy density window $d\varepsilon$. Dashed lines denote the average width σ of the initial state $|\Psi_0\rangle$ in the Hamiltonian H , providing an estimation of the eigenstates effectively contributing to the dynamics. As in Fig. S9, we restrict the analysis to 16-qubits, and re-scale the energy axis by displaying the energy density ε instead. (B) Average value of the ratio of adjacent gaps \bar{r} in the same $\gamma - \varepsilon$ space: large tilt potentials yield in uncorrelated eigenenergies such that the \bar{r}_ε within the small energy windows $d\varepsilon$ quickly drops to the Poisson value $r_P \simeq 0.39$, even before fragmentation takes place at larger γ 's.